

Quantifying vegetation indices using Terrestrial Laser Scanning: methodological complexities and ecological insights from a Mediterranean forest

William Rupert Moore Flynn¹, Harry Jon Foord Owen², Stuart William David Grieve^{1,3} and Emily Rebecca Lines²

¹School of Geography, Queen Mary University of London, Mile End Rd, Bethnal Green, London E1 4NS

²Department of Geography, University of Cambridge, Downing Place, Cambridge, CB2 3EN

³Digital Environment Research Institute, Queen Mary University of London, New Road, London, E1 1HH

Correspondence to: W. R. M. Flynn (w.r.m.flynn@qmul.ac.uk)

Abstract. Accurate measurement of vegetation density metrics including plant, wood and leaf area indices (PAI, WAI and LAI) is key to monitoring and modelling carbon storage and uptake in forests. Traditional passive sensor approaches, such as Digital Hemispherical Photography (DHP), cannot separate leaf and wood material, nor individual trees, and require many assumptions in processing. Terrestrial Laser Scanning (TLS) data offer new opportunities to improve understanding of tree and canopy structure. Multiple methods have been developed to derive PAI and LAI from TLS data, but there is little consensus on the best approach, nor are methods benchmarked as standard.

Using TLS data collected in 33 plots containing 2472 trees of five species in Mediterranean forests, we compare three TLS methods (*LiDAR Pulse*, *2D Intensity Image* and *Voxel-Based*) to derive PAI and compare with co-located DHP. We then separate leaf and wood in individual tree point clouds to calculate the ratio of wood to total plant area (α), a metric to correct for non-photosynthetic material in LAI estimates. We use individual tree TLS point clouds to estimate how α varies with species, tree height and stand density.

We find the *LiDAR Pulse* method agrees most closely with DHP, but is limited to single scan data so cannot determine individual tree properties, including α . The *Voxel-Based* method shows promise for ecological studies as it can be applied to individual tree point clouds. Using the *Voxel-Based* method, we show that species explain some variation in α , however, height and plot density were better predictors.

Our findings highlight the value of TLS data to improve fundamental understanding of tree form and function, but also the importance of rigorous testing of TLS data processing methods at a time when new approaches are being rapidly developed. New algorithms need to be compared against traditional methods, and existing algorithms, using common reference data. Whilst promising, our results show that metrics derived from TLS data are not yet reliably calibrated and validated to the extent they are ready to replace traditional approaches for large scale monitoring of PAI and LAI.

33 **1 Introduction**

34 Leaf Area Index (LAI), defined as half the amount of green leaf area per unit ground area (Chen and Black, 1992),
35 determines global evapotranspiration, phenological patterns and canopy photosynthesis, and is therefore an
36 essential climate variable (ECV), as well as a key input in dynamic global vegetation models (Sea et al., 2011;
37 Weiss et al., 2004). Accurate measurements of leaf, wood and plant area indices (LAI, WAI and PAI) have
38 historically been derived from labour intensive destructive sampling (Baret et al., 2013; Jonckheere et al., 2004),
39 so over large spatial or temporal scales these can only be measured indirectly, typically with remote sensing.
40 Large-scale remote sensing, using spaceborne and airborne instruments, has been widely used to estimate LAI
41 over large areas (Pfeifer et al., 2012), but requires calibration and validation using in situ measurements to
42 constrain information retrieval (Calders et al., 2018). Non-destructive in situ vegetation index estimates have
43 historically been made by measuring light transmission below the canopy and using simplifying assumptions
44 about canopy structure to estimate the amount of intercepting material (e.g. Beer-Lambert's law; Monsi and Saeki,
45 1953). The most common method, Digital Hemispherical Photography (DHP; Figure 1a), requires both model
46 assumptions and subjective user choices during data acquisition and processing in order to estimate both PAI and
47 LAI (Breda, 2003). DHP images are processed by separating sky from canopy, but not photosynthetic from non-
48 photosynthetic vegetative material, so additional assumptions are needed to calculate either LAI or WAI
49 (Jonckheere et al., 2004; Pfeifer et al., 2012). Separation of LAI from PAI can be achieved by removing or
50 masking branches and stems from hemispherical images (e.g. Sea et al., 2011; Woodgate et al., 2016), but is not
51 reliable when leaves are occluded by woody components (Hardwick et al., 2015). An alternative approach is to
52 take separate DHP measurements in both leaf on and leaf off conditions, and derive empirical wood to plant ratios
53 (WAI/PAI, α) (Leblanc and Chen, 2001), but this is not always practical, for example in evergreen forests. The
54 difficulty of separation means that studies often omit correcting for the effect of WAI on optical PAI
55 measurements altogether (Woodgate et al., 2016), but since woody components in the forest canopy can account
56 for more than 30% of PAI (Ma et al., 2016) this can introduce overestimation. Further, although DHP estimates
57 of LAI or PAI are valuable both for ecosystem monitoring and developing satellite LAI products (Hardwick et
58 al., 2015; Pfeifer et al., 2012), they are limited to sampling only at a neighbourhood or plot level (Weiss et al.,
59 2004), and cannot be used to measure individual tree LAI except for open grown trees (Béland et al., 2014).

60 The ratio of wood to total plant area, α , is known to be dynamic, changing in response to abiotic and biotic
61 conditions. For example, the Huber value (sapwood to leaf area ratio, a related measure to α) may vary according
62 to water availability (Carter and White, 2009). Leaf area may therefore be indicative of the drought tolerance level
63 of a tree, with more drought tolerant species displaying a lower leaf area, reducing the hydraulic conductance of
64 the whole tree and therefore increasing its drought tolerance (Niinemets and Valladares, 2006). α has been
65 hypothesised to increase with the size of a tree in response to the increased hydraulic demand associated with
66 greater hydraulic resistance of tall trees (Magnani et al., 2000) and higher transpiration rates of larger LAI
67 (Battaglia et al., 1998; Phillips et al., 2003). Stand density may also impact α (Long and Smith, 1988; Whitehead,
68 1978), as increased stand level water use scales linearly with LAI (Battaglia et al., 1998; Specht and Specht, 1989),
69 reducing water availability to individual trees competing for the same resources (Jump et al., 2017). Large scale
70 quantification of α or Huber value, however, is difficult as studies usually rely on a small number of destructively
71 sampled trees (e.g. Carter and White, 2009; Magnani et al., 2000), litterfall traps (e.g. Phillips et al., 2003) or

72 masking hemispherical images (e.g. Sea et al., 2011; Woodgate et al., 2016). These approaches are only applicable
73 on a small to medium scale, and in the case of image masking, cannot differentiate between individuals. Variation
74 in α , for example by species and or stand structure, is therefore largely unknown.

75 **1.1 TLS methods for calculating PAI, LAI and WAI**

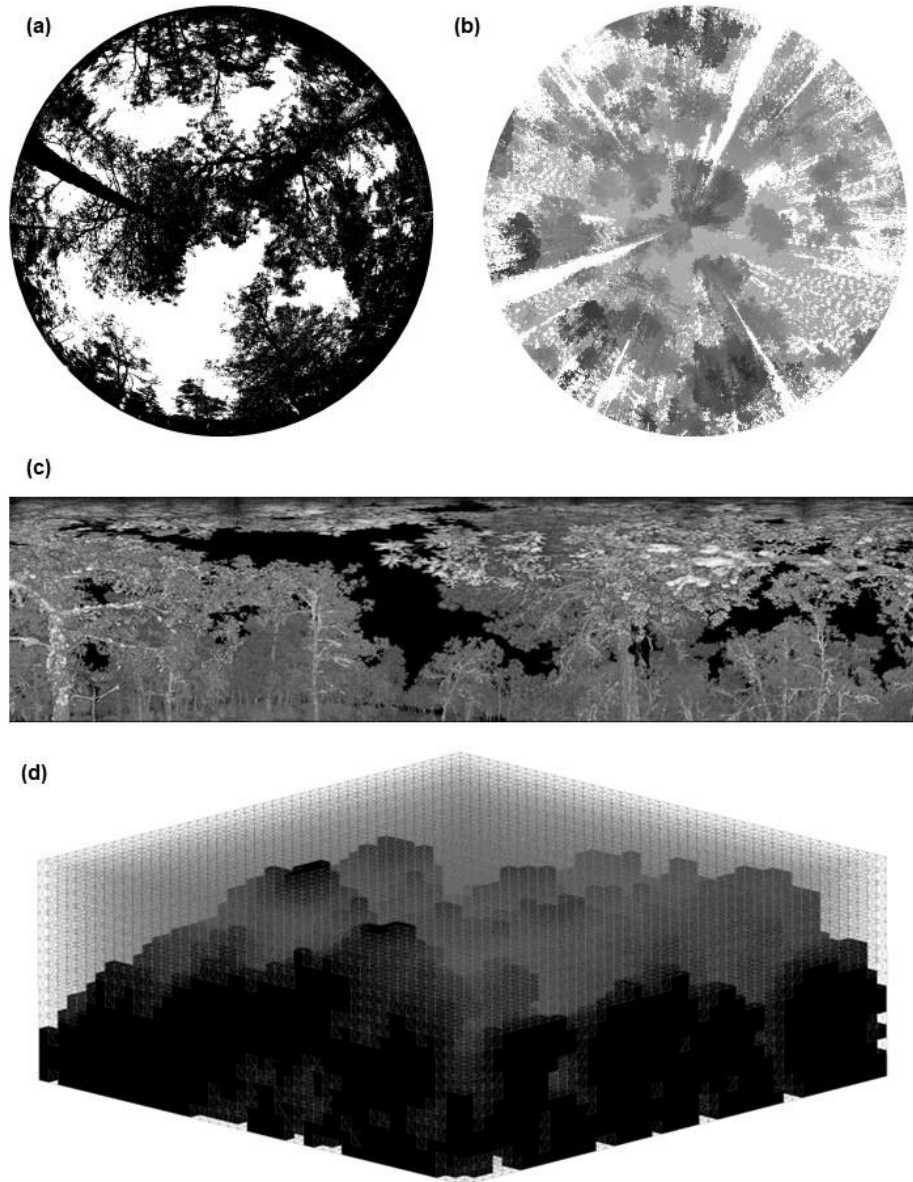
76 Terrestrial Laser Scanning (TLS) generates high-resolution 3D measurements of whole forests and individual
77 trees (Burt et al., 2018; Disney, 2018), leading to the development of completely new monitoring approaches to
78 understand the structure and function of ecosystems (Lines et al., 2022). Unlike traditional passive sensors, TLS
79 can estimate PAI, WAI, and LAI for both whole plots and individual tree point clouds (Calders et al., 2018), and
80 is unaffected by illumination conditions. This has led to the development of several methods for processing TLS
81 data to extract the key metrics PAI, WAI and LAI (e.g. Hosoi and Omasa, 2006; Jupp et al., 2008; Zheng et al.,
82 2013). However, intercomparison studies of algorithms and processing approaches to derive the same metrics
83 from different TLS methods are lacking. TLS methods for extracting PAI, LAI and WAI can be broadly
84 categorised into two types: (1) LiDAR return counting, using single scan data (e.g., the *LiDAR Pulse* method;
85 Jupp et al., 2008, and *2D Intensity Image* method; Zheng et al., 2013) and (2) point cloud voxelisation, usually
86 using co-registered scans (e.g., the *Voxel-Based* method; Hosoi and Omasa, 2006).

87 The *LiDAR Pulse* method (Jupp et al., 2008; Figure 1b) estimates gap fraction (P_{gap}) using single scan data, as a
88 function of the total number of outgoing LiDAR pulses from the sensor and the number of pulses that are
89 intercepted by the canopy. This method, which eliminates illumination impacts associated with the use of DHP
90 (Calders et al., 2014), has been implemented in the python module, *PyLidar* (www.pylidar.org) and the R package,
91 *rTLS* (Guzman, et al. 2021). Using the *LiDAR Pulse* method, Calders et al. (2018) compared PAI estimates from
92 two ground-based passive sensors (LiCOR LAI-2000 and DHP) with TLS data collected with a RIEGL VZ-400
93 TLS in a deciduous woodland, and found the two passive sensors underestimated PAI values compared to TLS,
94 with differences dependent on DHP processing and leaf on/off conditions.

95 The *2D Intensity Image* method (Zheng et al., 2013; Figure 1c), also uses raw single scan TLS point clouds, but,
96 unlike the *LiDAR Pulse* method, converts LiDAR returns into 2D panoramas where pixel values represent return
97 intensity. PAI is estimated by classifying pixels as sky or vegetation, based on their intensity value, to estimate
98 P_{gap} , and then applying Beer-Lambert's law. Like the *LiDAR Pulse* method, this approach has been shown to
99 generate higher PAI estimates than DHP (Calders et al., 2018; Woodgate et al., 2015; Grotti et al., 2020), with
100 differences attributed to the greater pixel resolution and viewing distance of TLS resolving more small canopy
101 details (Grotti et al., 2020).

102 The *Voxel-Based* method (Figure 1d) estimates PAI by segmenting a point cloud into voxels and either simulating
103 radiative transfer within each cube (Béland et al., 2014; Kamoske et al., 2019), or classifying voxels as either
104 containing vegetation or not, and dividing vegetation voxels by the total number of voxels (Hosoi and Omasa,
105 2006; Itakura and Hosoi, 2019; Li et al., 2017). Crucially, this method may be applied to multiple co-registered
106 scan point clouds and so can be used to calculate PAI for both whole plots and individual, segmented TLS trees.
107 However, PAI estimates derived using the voxel method are highly dependent on voxel size (Calders et al., 2020).
108 Using a radiative transfer approach, Béland et al. (2014) demonstrated that voxel size is dependent on canopy
109 clumping, radiative transfer model assumptions and occlusion effects, making a single, fixed choice of voxel size

110 for all ecosystem types, scanners or datasets impossible. To test various approaches to selecting voxel size using
111 a voxel classification approach, Li et al. (2016) matched voxel size to point cloud resolution, individual tree leaf
112 size, and minimum beam distance and tested against destructive samples, finding that voxel size matched to point
113 cloud resolution had the closest PAI values to destructive samples. The *LiDAR Pulse* method and *2D Intensity*
114 *Image* method both use single scan data. However, to generate robust estimates of canopy properties that avoid
115 errors from occlusion effects, multiple co-registered scans taken from different locations are likely needed (Wilkes
116 et al., 2017). Further, both these methods require raw unfiltered data to accurately measure the ratio of pulses
117 emitted from the scanner and number of pulses that are intercepted by vegetation. This means “noisy” points



118 caused by backscattered pulses (Wilkes et al., 2017) are included in analyses, potentially leading to higher PAI
119 estimates. However, the *LiDAR Pulse* and *2D Intensity Image* methods may introduce fewer estimation errors
120 compared to DHP, which is influenced by differences in sky illumination conditions and camera exposure (Weiss
121 et al., 2004).

122

123

124 **Figure 1: Visual representation of the four methods for PAI and WAI estimation used in this study: (a) a binarised**

125 digital hemispherical photograph (DHP), (b) TLS raw single scan point cloud, for the *LiDAR Pulse* method (Jupp et

126 al., 2008). Image shows a top-down view of raw point cloud and greyscale represents low (grey) and high (black) Z

127 values, (c) TLS 2D intensity image for the *2D Intensity Image* method (Zheng et al., 2013), (d) Voxelised co-registered

128 whole plot point cloud for the *Voxel-Based* method (Hosoi and Omasa, 2006), showing a representative schematic of

129 cube voxels with edge length of 1m, voxelised using the *R* package *VoxR* (Lecigne et al., 2018). Solid black voxels are

130 classified as containing vegetation (filled) and voxels outlined with grey lines are voxels classified as empty.

131 **1.2 Scope and aims**

132 The aims of this study are twofold: the first aim is to compare three TLS methods for estimating PAI with

133 traditional DHP. The second aim of this study is to use TLS to understand drivers of individual tree α variation.

134 In this study we use a dataset of 528 co-located DHP and high-resolution TLS scans from 33 forest plots to

135 compare DHP derived PAI (PAI_{DHP}) with estimates from three methods to estimate PAI from TLS data (PAI_{TLS}):

136 the *LiDAR Pulse* method; the *2D Intensity Image* method and the *Voxel-Based* method (Figure 1). We use a dataset

137 collected from a network of pine/oak forest plots in Spain (Owen et al., 2021) and ask (1) are the three TLS

138 methods able to reproduce PAI_{DHP} estimates at single scan and whole plot level? (2) does α , calculated from the

139 *Voxel-Based* method on individual tree point clouds, vary with species and tolerance to drought? and (3) does α

140 scale with height and stand density?

141 **2. Methods**

142 **2.1 Study site**

143 We collected TLS and DHP data from 29 plots in Alto Tajo Natural Park ([40°41'N, 02°03'W](#); FunDIV –

144 Functional Diversity plots; see Baeten et al. (2013) for a detailed description of the plots) and four plots in Cuellar

145 ([41°23'N 4°21'W](#)) in June - July 2018 (see Owen et al. (2021) for full details) (Figure A1). Plots contained two

146 oak species: semi-deciduous *Q. faginea* and evergreen *Q. ilex*, and three pine species: *P. nigra*, *P. pinaster* and *P.*

147 *sylvestris*. *P. sylvestris* is the least drought tolerant species, followed by *P. nigra*, *Q. faginea*, *Q. ilex*; shade

148 tolerance follows the same ranking (Niinemets and Valladares, 2006; Owen et al., 2021). Although not

149 quantitatively ranked, *P. pinaster* has been shown to be very drought tolerant, appearing in drier areas than the

150 other species (Madrigal-González et al., 2017). The area is characterised by a Mediterranean climate (altitudinal

151 range 840 – 1400 m.a.s.l.) (Jucker et al., 2014; Madrigal-González et al., 2017). In addition to the five main canopy

152 tree species, plots contained an understory of *Juniperus thurifera* and *Buxus sempervirens* (Kuusk et al., 2018).

153 **2.2 Field protocol**

154 In each of the 33 plots of size 30 x 30 m, we collected TLS scans on a 10 m grid, making 16 scan locations

155 following Wilkes et al. (2017) to minimise occlusion effects associated with insufficient scans. We used a Leica

156 HDS6200 TLS set to super high resolution (3.1 x 3.1mm resolution at 10 m with a beam divergence of ≤ 5 mm at

157 50 m; scan time 6m 44 s; see Owen et al. (2021)). At each of the 528 scan locations and following the protocol in

158 Pfeifer et al. (2012), we captured co-located DHP images with three exposure settings (automatic and \pm one stop

159 exposure compensation), levelling a Canon EOS 6D full frame DSLR sensor with a Sigma EX DG F3.5 fisheye

160 lens, mounted on a Vanguard Alta Pro 263AT tripod.

161 **2.3 Calculation of single scan and whole plot PAI using DHP data**

162 For each of the red-green-blue (RGB) DHP images we extracted the blue band for image thresholding, as this best
163 represents sky/vegetation contrast (Pfeifer et al., 2012). For each plot, we picked the exposure setting that best
164 represented sky/ vegetation difference based on pixel brightness histograms of four sample locations indicative of
165 the plot. We carried out automatic image thresholding using the Ridler and Calvard method (1978), to create a
166 binary image of sky and vegetation, avoiding subjective user pixel classification (Jonckheere et al., 2005). We
167 calculated PAI from the binary image, limiting the field of view to a 5° band centred on the hinge angle of 57.5°
168 (55° – 60°). The hinge angle has a path length through the canopy twice the canopy height, so the band around it
169 is an area of significant spatial averaging taken as representative of canopy structure of the area (Calders et al.,
170 2018; Jupp et al., 2008). From the binarised hinge angle band we calculated P_{gap} as the number of sky pixels
171 divided by the total number of pixels and PAI using an inverse Beer-Lambert law equation (Monsi and Saeki,
172 1953). We calculated whole plot PAI as the arithmetic mean of the 16 plot scan location PAI estimates. As this
173 value does not correct for canopy clumping, it is better described as effective PAI, rather than true PAI (Woodgate
174 et al., 2015). However, as the TLS and DHP methods we apply here account for canopy clumping differently, we
175 compared effective values and here-on refer to effective PAI as PAI (Calders et al., 2018). DHP images used in
176 this study are freely available (see Flynn et al., 2023).

177 **2.4 Calculation of single scan and whole plot PAI from TLS data**

178 To calculate PAI using the *LiDAR Pulse* method (Jupp et al., 2008), we calculated P_{gap} for a single scan (Figure
179 1b) by summing all returned laser pulses and dividing by the number of total outgoing pulses, following Lovell et
180 al. (2011; see Eq. 7 in that study), and then estimated PAI following Jupp et al. (2008; see Eq. 18 in that study),
181 setting the sensor range to 5° around the hinge angle as before (55° – 60°). Single scan PAI was taken as the
182 cumulative sum of PAI values estimated by vertically dividing the hinge region into 0.25 m intervals (Calders et
183 al., 2014). We implemented the *LiDAR Pulse* method using the open-source *R* (R Core Team, 2020) package,
184 *rTLS* (Guzmán and Hernandez, 2021).

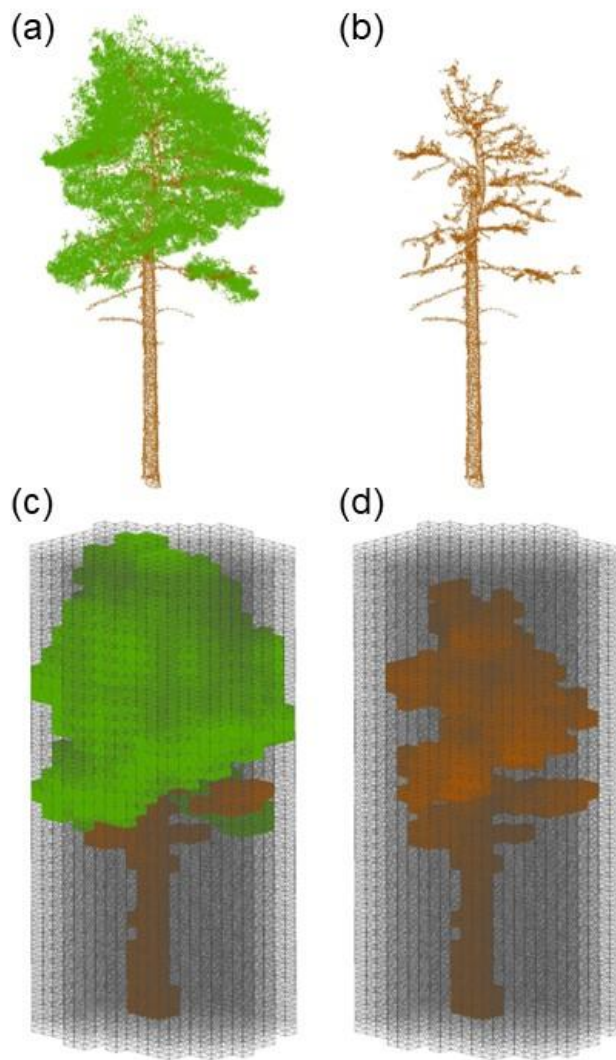
185 To calculate PAI using the *2D Intensity Image* method (Zheng et al., 2013), we converted 3D TLS point cloud
186 data from all 528 scan locations into polar coordinates, scaled intensity values to cover the full 0-255 range (Figure
187 1c) and rasterised into a 2D intensity image using the open-source *R* package, *raster* (Hijmans, 2022). We cut the
188 2D intensity image to a 5° band around the hinge angle (55 °– 60°) and classified sky and vegetation pixels in each
189 image using the Ridler and Calvard method (1978). We calculated P_{gap} as the number of pixels classified as sky
190 divided by the total number of pixels and derived PAI with an inverse Beer-Lambert law equation (Monsi and
191 Saeki, 1953).

192 Following the same approach as applied to our DHP data, we calculated whole plot PAI for the *LiDAR Pulse* and
193 *2D Intensity Image* methods as the arithmetic mean of the 16 plot scan location PAI estimates.

194 To calculate PAI using the *Voxel-Based* method, we followed a voxel classification approach (Hosoi and Omasa,
195 2006), downsampling the point cloud to 0.05 m to aid computation time and matching the voxel size to the
196 resolution of the point cloud, following Li et al. (2016), who showed that matching the voxel size to the point
197 cloud point to point minimum distance (resolution) increases accuracy as small canopy gaps are not included in
198 voxels classified as vegetation. We chose to use a voxel classification approach (rather than a radiative transfer

199 based one) as this method is widely applicable to a range of TLS systems and levels of processing, as well as
200 providing explicit guidance on voxel size selection, which is known to impact derived PAI estimates (Li et al.,
201 2016). We re-combined individually segmented trees, filtered for noise using a height-dependent statistical filter
202 (see Owen et al., 2021) back into whole plot point clouds and voxelised them using the open source *R* package,
203 *VoxR* (Lecigne et al., 2018), with a full grid covering the minimum to maximum XYZ ranges of the plot. We
204 classified any voxel containing > 0 points as vegetation (“filled”), and empty voxels as gaps. We then split the
205 voxelised point cloud vertically into slices one voxel high. Within each slice, the contact frequency is calculated
206 as the fraction of filled to total number of voxels. We then multiplied the contact frequency by a correction factor
207 for leaf inclination, set at 1.1 (Li et al., 2017), and whole plot PAI was calculated as the sum of all slices’ contact
208 frequencies.

209 **2.5 Calculation of individual tree PAI, WAI and α using the voxel-based method**



210 **Figure 2: Visualisation of the workflow for applying the Voxel-Based method to estimate individual-tree PAI, WAI and**
211 **α . (a) Individual tree point cloud; (b) separated leaf off (wood) individual tree point cloud; (c) voxelised individual tree**
212 **point cloud; (d) voxelised wood cloud. Coloured voxels (green represents leaf and brown represents wood) are filled**
213 **voxels and grey lines are empty voxels. Empty voxels occupy the space within the projected crown area of the tree.**
214 **Image shows schematic of point cloud voxelised with cube voxels with edge length of 0.5 m. Panels (a) and (b) show**
215 **wood and leaf separation of an example *P. sylvestris*, carried out using *TLSeparation* (Vicari et al., 2019). Point cloud**

216 voxelisation was carried out using modified functions from *R* package *VoxR* (Lecigne et al., 2018). Note that our method
217 used voxel sizes at the resolution of the cloud (0.05 m), but here we present an image with larger voxels to ease visual
218 interpretation.

219 As the only method using multiple co-registered scans, the *Voxel-Based* method is only method compared in this
220 study capable of deriving PAI, WAI and LAI of segmented individual tree point clouds. We estimated PAI and
221 WAI for 2472 individual trees segmented from co-registered point clouds following a similar method to the whole
222 plot point cloud. We used individual tree point clouds downsampled to 0.05 m, to aid computation time, and
223 segmented using the automated tree segmentation program *treeseg* (Burt et al., 2019), implemented in C++, by
224 Owen et al. (2021) for that study. Individual segmented tree data used in this study are freely available (see Owen
225 et al., 2022).

226 To estimate PAI, WAI and α for each tree, we used individual tree point clouds wood – leaf separated by Owen
227 et al. (2021) using the open source Python library *TLSeparation* (Vicari et al., 2019), and then used the separated
228 wood point clouds to calculate WAI. *TLSeparation* assigns points as either leaf or wood, iteratively looking at a
229 predetermined number of nearest neighbours (knn). The knn of each iteration is directly dependent on point cloud
230 density, since high density point clouds will require higher a knn (Vicari et al., 2019). The utility package in
231 *TLSeparation* was used to automatically detect the optimum knn for each tree point cloud.

232 To voxelize individual tree complete (Figure 2a) and wood only (Figure 2b) point clouds, we used a modified
233 approach based on Lecigne et al. (2018), voxelising within the projected crown area of the whole tree point cloud
234 (Figure 2c) to calculate PAI. In the same way as for PAI, we calculated WAI using the separated wood point cloud
235 within the projected crown area of the whole tree (Figure 2d; using the whole crown and not just the wood point
236 cloud), and derived α for each tree as WAI/PAI , allowing a comparison with existing literature estimating α for a
237 range of ecosystems, (Sea et al., 2011; Woodgate et al., 2016).

238 2.6 Statistical Analyses

239 We tested the relationships between PAI_{TLS} and PAI_{DHP} estimates using Standardised Major Axis (SMA) using
240 the open source *R* (R Core Team, 2020) package, *smatr* (Warton et al., 2012). SMA is an approach to estimating
241 a line of best fit where we are not able to predict one variable from another (Warton et al., 2006); we chose SMA
242 because we do not have a ‘true’ validation dataset, so avoid assuming either DHP or any of the TLS methods
243 produces the most accurate results. For each TLS method, we assessed the relationship with DHP using the
244 coefficient of determination and RMSE. We chose to compare PAI values rather than WAI or LAI as to do so
245 would mean an additional correction for non-photosynthetic elements, which each method does in different ways,
246 so introducing further source of uncertainty and limiting our ability to fairly compare processing approaches. To
247 further understand observed drivers of variance in PAI, we tested the relationship between PAI and whole plot
248 crown area index, CAI, a proxy measure of stand density and local competition (Caspersen et al., 2011; Coomes
249 et al., 2012). We calculated CAI as the sum of TLS-derived projected crown area, divided by the plot area (Owen
250 et al., 2021).

251

252 To test if α differs by species, we used linear mixed models (LMMs) in the *R* package, *lme4* (Bates et al., 2015).
253 We included an intercept only random plot effect to account for local effects on α :

254

255 $\alpha_{i,sj} = \varphi_s + Plot_j,$ (1)

256

257 here, α_i is α of an individual of species s , in plot j , and φ_s is the parameter to be fit. To test the effect of stand
258 structure and tree height on α , we fit relationships separately for each species, again including a random plot
259 effect:

260

261 $\alpha_{i,sj} = \varphi_s + b_s H_i + c_s CAI_j + Plot_{sj}.$ (2)

262

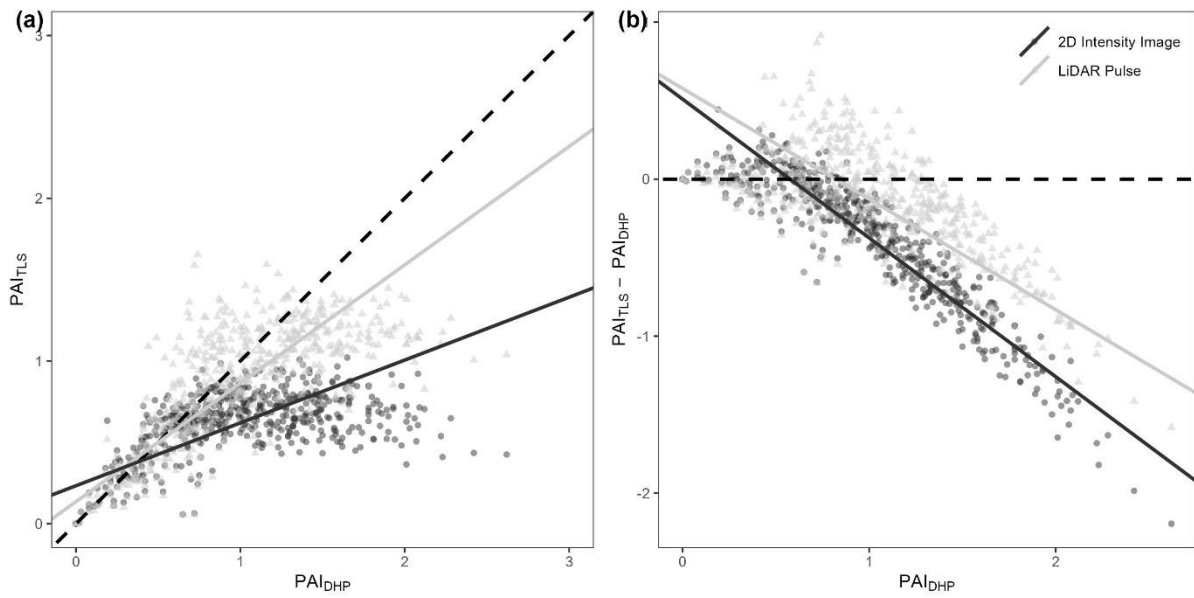
263 here H_i is the height of the tree, CAI_j is the crown area index for the plot, with other parameters as before.

264 For each species' model (equation 2), we calculated the intra-class correlation coefficient (ICC). The ICC, similar
265 to coefficient of determination, quantifies the amount of variance explained by the random effect in a linear mixed
266 model (Nakagawa et al., 2017).

267 **3. Results**

268 **3.1 Comparison of plant area index estimated by DHP and single scan TLS**

269 Of the two single scan TLS methods tested (*LiDAR Pulse* method and *2D Intensity Image* method), we found that
270 the relationship between PAI estimated using the *LiDAR Pulse* method and PAI_{DHP} , had a higher R^2 than the *2D*
271 *Intensity Image* method (SMA; *LiDAR Pulse* method $R^2 = 0.50$, slope = 0.73, $p < 0.001$, RMSE = 0.14, and *2D*
272 *Intensity Image* method $R^2 = 0.22$, slope = 0.38, $p < 0.001$, RMSE = 0.39, respectively, Figure 3a). At larger PAI
273 values, both TLS methods underestimated PAI relative to DHP (Figure 3b). We found statistically significant
274 negative correlations between residuals and DHP for both methods (SMA; *2D Intensity Image* method residuals
275 $R^2 = 0.85$, slope = -0.88, $p < 0.01$; *LiDAR Pulse* method residuals $R^2 = 0.47$, slope = -0.70, $p < 0.01$; Figure 3b).
276 The *2D Intensity Image* method showed larger underestimation at higher PAI_{DHP} values, suggesting this method
277 may saturate sooner for higher PAI values than either DHP or the *LiDAR Pulse* method (Figure 3b).



278

279 **Figure 3: Comparison of single scan PAITLS and PAIDHP estimates, for all 528 scan locations (16 per plot). (a) The**
 280 **correlation between DHP derived PAI with PAI derived using the 2D Intensity Image method $R^2 = 0.22$, slope = 0.38,**
 281 **$p < 0.001$, RMSE = 0.39 (circles), and LiDAR Pulse method $R^2 = 0.50$, slope = 0.73, $p < 0.001$, RMSE = 0.14 (triangles).**
 282 **Dashed line in panel (a) represents 1:1 relationship. (b) The difference between PAITLS and PAIDHP estimates for the**
 283 **2D Intensity Image method, and LiDAR Pulse method. Dashed line in panel (b) represents 0. Solid lines show**
 284 **statistically significant relationships fitted using SMA ($p < 0.01$).**

285 **3.2 Comparison of whole plot plant area index estimated using TLS and DHP and the effect of plot structure**
 286 **on PAI**

287 We found statistically significant correlations between whole plot PAITLS values and PAIDHP for all three TLS
 288 methods (Figure 4). As for single scans, the *LiDAR Pulse* method showed the closest agreement to PAIDHP, here
 289 compared to both the *Voxel-Based* and *2D Intensity Image* methods (SMA; *LiDAR Pulse* method $R^2 = 0.66$, slope
 290 = 0.82, $p < 0.01$, RMSE = 0.14; *Voxel-Based* method $R^2 = 0.39$, slope = 2.76, $p < 0.01$, RMSE = 0.88; *2D Intensity*
 291 *Image* method $R^2 = 0.35$, slope = 0.36, $p < 0.01$, RMSE = 0.39, respectively; Figure 4a). The *2D Intensity Image*
 292 method and *LiDAR Pulse* method consistently underestimated PAI compared to DHP, whilst the *Voxel-Based*
 293 method underestimated in plots with lower PAIDHP and overestimated in plots with higher PAIDHP. The *Voxel-*
 294 *Based* method's high PAI values compared to other methods is likely due to its use of multiple co-registered scans
 295 reducing occlusion effects prevalent in single scan data.

296 To assess the effect of plot structure on variation in TLS derived PAI, we compared PAITLS estimates CAI (Figure
 297 4b). We found a significant positive relationship between CAI and PAI estimated using each of the *LiDAR Pulse*
 298 method, the *Voxel-Based* method, and DHP (SMA; *LiDAR Pulse* method $R^2 = 0.79$, slope = 1.69, $p < 0.01$; *Voxel-*
 299 *Based* method $R^2 = 0.76$, slope = 5.72, $p < 0.01$; *2D Intensity Image* method $R^2 = 0.15$, slope = 0.76, $p < 0.05$;
 300 DHP $R^2 = 0.46$, slope = 2.07, $p < 0.01$, respectively; Figure 4b), where the *2D Intensity Image* method shows
 301 signs of saturation at medium CAI values (Figure 4b).

302

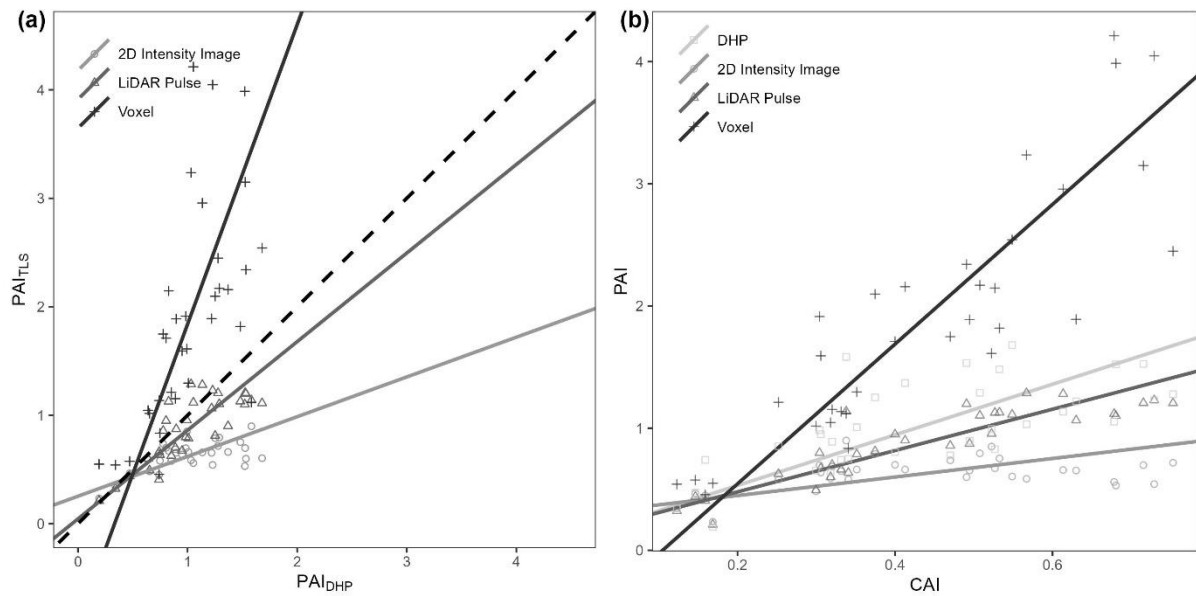
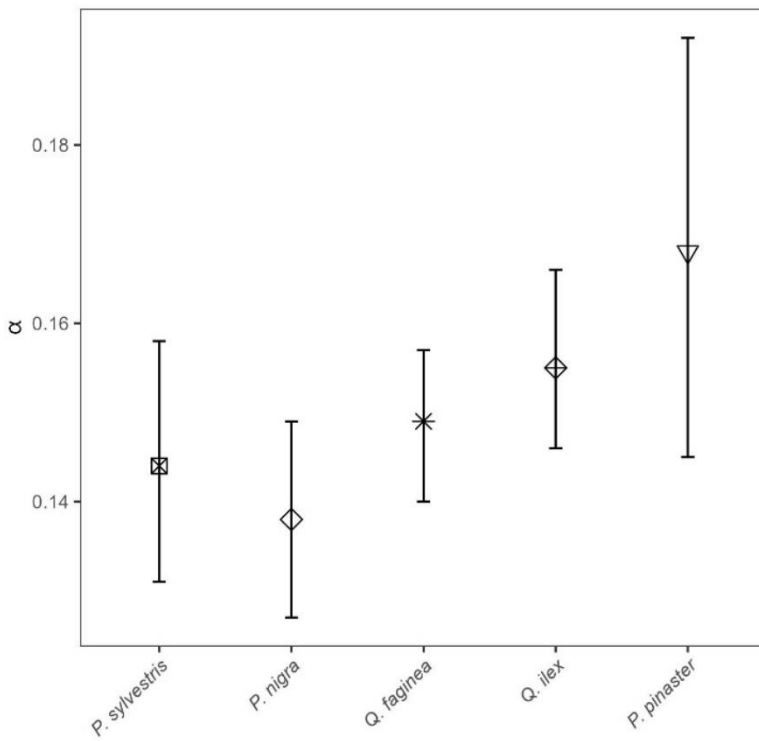


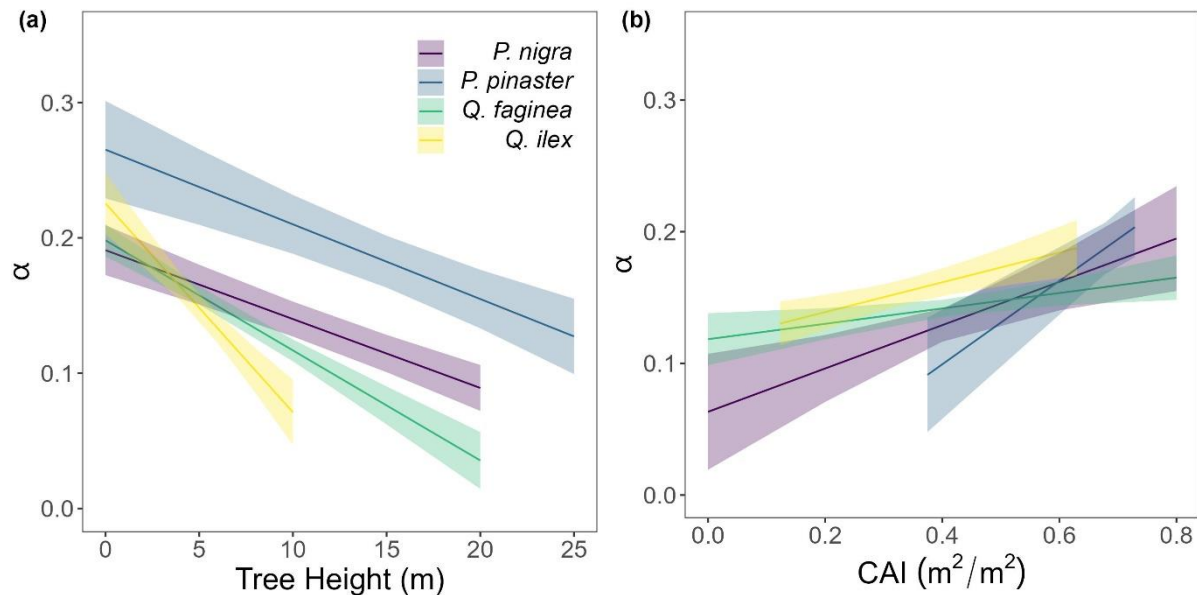
Figure 4: Comparison of plot level PAI_{TLS} vs PAI_{DHP}, and CAI vs PAI estimates for all 33 plots. (a) The correlation between DHP derived PAI and PAI derived using 2D Intensity Image $R^2 = 0.35$, slope = 0.36, $p < 0.01$, RMSE = 0.39 (circle), LiDAR Pulse $R^2 = 0.66$, slope = 0.82, $p < 0.01$, RMSE = 0.14 (triangle) and Voxel-Based $R^2 = 0.39$, slope = 2.76, $p < 0.01$, RMSE = 0.88 (cross) methods (b) The correlation between TLS derived CAI and PAI derived using DHP $R^2 = 0.46$, slope = 2.07, $p < 0.01$ (square), 2D Intensity Image $R^2 = 0.15$, slope = 0.76, $p < 0.05$ (circle) LiDAR Pulse $R^2 = 0.79$, slope = 1.69, $p < 0.01$ (triangle) and Voxel-Based $R^2 = 0.76$, slope = 5.72, $p < 0.01$ (cross) methods. Lines show statistically significant relationships fitted using SMA ($p < 0.01$). Dashed line in panel (a) represents 1:1 relationship.

3.4 Influence of species, tree height and CAI on α

To understand drivers of variance in α , we used individual tree PAI and WAI, calculated using the *Voxel-Based* method to test the relationship between species and α , and height/ CAI and α . We found that more drought tolerant species generally had higher α values than less drought tolerant species (Table B1; Figure 5), however, confidence intervals were wide and overlapping, suggesting that species is not a strong predictor of variation in α . We found a statistically significant negative effect of height ($p < 0.001$; Table B2; Figure 6a) and positive effect of CAI ($p < 0.01 - 0.05$; Table B2; Figure 6b) on α for all species apart from *P. sylvestris*. α decreased more rapidly with height and increased less rapidly with CAI for oaks than pines. Statistically significant ICC values were higher for *P. nigra* (ICC = 0.211; Table B2) than *P. pinaster*, *Q. faginea* and *Q. ilex* (ICC = 0.036; 0.060; 0.070, respectively), showing that more α variation is explained by the random plot effect in *P. nigra* than the other species. *P. pinaster* has a wider confidence interval (Figure 5), possibly explained by its lower sample size. To understand drivers of variance in WAI we carried out additional analysis to test the relationship between WAI and species, height, CAI, and PAI, and presented these results in Appendix C (Figure C3; Tables C3, C4).



323
324 **Figure 5:** Linear mixed model derived α values (ϕ , equation 1) for all 2472 individual trees of species *P. sylvestris*, *P.*
325 *nigra*, *Q. faginea*, *Q. ilex* and *P. pinaster*. Error bars represent 95% confidence intervals. Species are listed left to right
326 from low – high drought tolerance, with the exception of *P. pinaster*, for which drought tolerance index has not been
calculated in the literature. Drought tolerance rankings are taken from Niinemets and Valladares (2006).



327
328 **Figure 6:** Variation in α for each species: *Pinus nigra*, *P. pinaster*, *Q. faginea* and *Q. ilex* with (a) height and (b) plot
329 CAI. Lines represent statistically significant linear mixed models (equation 2; significance levels from $p < 0.001$ to $p <$
0.05). Ribbons represent 95% confidence intervals. The model for *P. sylvestris* was not statistically significant.

330
331
332

333 **4. Discussion**

334 **4.1 Comparison of approaches to deriving PAI from remote sensed data**

335 We found substantial differences in PAI values estimated from TLS and DHP and from different TLS processing
336 methods (Figures 3 and 4). Further, differences between TLS methods varied across plot structure, with the
337 greatest differences between methods in plots with high CAI, and therefore high canopy density. Although
338 previous studies have presented TLS as an improvement over DHP due to its independence of illumination and
339 sky conditions during the data acquisition phase, and ability to resolve fine-scale canopy elements and gaps
340 (Calders et al., 2018; Grotti et al., 2020; Zhu et al., 2018), we have shown that there is large variability between
341 TLS processing methods in Mediterranean forests. Rigorous intercomparison of approaches, ideally using
342 standard benchmarking TLS datasets, and destructive sampling, would improve trust and reliability of TLS
343 algorithms.

344 We found the *LiDAR Pulse* method (Jupp et al., 2008) to have the best agreement with DHP for both whole plot
345 and single scan PAI estimates. In contrast to previous studies comparing PAI_{TLS} with PAI_{DHP} (Calders et al.,
346 2018; Grotti et al., 2020; Woodgate et al., 2015), we found that the *LiDAR Pulse* and *2D Intensity Image* methods
347 underestimated PAI compared to DHP, except at very low PAI values ($PAI_{TLS} < 0.5$). Quantification of PAI from
348 DHP may introduce additional sources of error, for example, its relatively lower resolution compared to TLS
349 could lead to mixed pixels that have a greater chance of misclassification of sky as vegetation (Jonckheere et al.,
350 2004). This effect could be enhanced in a Mediterranean forest as trees in drier climates tend to have smaller
351 leaves (Peppe et al., 2011), leading to more small canopy gaps that TLS may resolve where DHP cannot. Further,
352 although we took steps to reduce the error introduced at DHP data acquisition and processing steps, including
353 using automatic thresholding and collecting images with multiple exposures, DHP processing requires both model
354 and user assumptions that can impact results. For example, PAI_{DHP} estimates are highly sensitive to camera
355 exposure; increasing one stop of exposure can result in 3 – 28% difference in PAI and use of automatic exposure
356 can result in up to 70% error (Zhang et al., 2005).

357 We found the *Voxel-Based* method overestimated PAI values compared to the other methods at the whole plot
358 level. This is likely due to the method's use of co-registered scans, rather than averaged single scan PAI values,
359 since co-registered scans will reduce occlusion effects prevalent in single scan data that could lead to an
360 underestimation of PAI (Wilkes et al., 2017). The *Voxel-Based* method is, however, sensitive to voxel size (Li et
361 al., 2016), and larger voxels lead to larger PAI estimates as they are unable to capture all of the intricate details of
362 canopy structure; we chose a voxel size of 0.05 m to match the minimum distance between points in our
363 downsampled dataset. However, the *Voxel-Based* method is a memory intensive approach to calculating PAI, and
364 smaller voxels have higher memory requirements. We picked this data resolution, and therefore voxel size, to
365 balance the need to capture fine-scale canopy details against memory requirements for running the method on
366 many large plot point clouds. Voxel size could have been chosen based on estimates' match to DHP, but this
367 would assume (1) that DHP estimates are most accurate, and (2) that DHP data are always available, limiting the
368 wider applicability of our findings. Understanding which method is over- or underestimating would require a
369 destructively sampled dataset for validation, which was not possible for this study (or most ecosystems). However,
370 other studies using voxel approaches have found that although these produce high LAI values for individual trees,
371 these are underestimates compared with destructive samples (Li et al., 2016). Regardless, PAI and LAI estimates

372 using a *Voxel-Based* approach are highly dependent on voxel size (Li et al., 2016), and future work should test
373 the influence of voxel size on PAI estimates, using destructive samples in a range of environments.

374 The relationship between the *LiDAR Pulse* method and TLS derived CAI had the highest R^2 , demonstrating that
375 the method is well suited to measuring PAI across the range of plot CAI values used in this study. Although the
376 *2D Intensity Image* method can tackle the significant challenges presented by edge effects and partial beam
377 interceptions, particularly present in phase-shift systems (Grotti et al., 2020), our results suggest this method has
378 a lower performance ability, with saturation occurring sooner than all other methods in dense forests (Figures 3
379 and 4). The *2D Intensity Image* method uses the same raw single scan data as the *LiDAR Pulse* method, so the
380 better performance from the latter is likely due to the method's use of vertically resolved gap fraction; both the
381 *LiDAR Pulse* method and *Voxel-Based* method account for the vertical structure of the canopy by summing
382 vertical slices through the canopy.

383 **4.2 α variation between species and plot**

384 We used the *Voxel-Based* method to investigate individual tree α variation between species and across structure,
385 as this was the only approach we compared that could be applied to single tree point clouds which are leaf-wood
386 separated. We found α values obtained were within the range of values obtained from destructive approaches (0.1
387 – 0.6, Gower et al., 1997). The drought and shade intolerant *P. nigra* showed stronger variability in α across plots
388 (higher ICC value, Table B2) than other species, suggesting its wood – leaf ratio may be more sensitive to site
389 factors. However, as the plots measured in this study vary in both abiotic conditions (altitude, aspect, slope,
390 wetness) as well as species composition, stem density and canopy cover, there may be other drivers of variation
391 in α values.

392 We found some evidence that species with higher drought tolerance had higher α values (Figure 5; Table B1),
393 however, confidence intervals were wide, suggesting a weak relationship. There is evidence that trees that tolerate
394 water limited environments have a lower leaf area (Battaglia et al., 1998; Mencuccini and Grace, 1995), so higher
395 α values may reflect maintenance of homeostasis of leaf water use through adjustment of wood to leaf area ratio
396 (Carter and White, 2009; Gazal et al., 2006). The potential for a tree to lose water is mostly regulated through leaf
397 traits including stomatal conductance and leaf area, and both stand (Battaglia et al., 1998; Specht and Specht,
398 1989) and individual tree (Mencuccini, 2003) water use have been found to scale linearly with LAI, with drought
399 often mitigated through leaf shedding (López et al., 2021).

400 **4.3 Tree stature and stand density drives α variation**

401 Although species had a weak relationship with α , tree height and plot CAI had a statistically significant
402 relationship with α ($p < 0.001$ – $p < 0.05$) for all species, showing the importance of local stand structure on leaf
403 and woody allocation. We found that α scaled negatively with height for all species apart from *P. sylvestris*,
404 suggesting that in this environment, taller trees generally have a lower proportion of wood to plant area index than
405 shorter ones. *P. sylvestris*, which is at the edge of its geographical range and physiological limits (Castro-Díez et
406 al., 1997; Owen et al., 2021), showed no significant relationship between height and α . We found that α scaled
407 positively with plot level CAI for all species apart from *P. sylvestris*, that is, trees growing in denser plots have a
408 higher α . This supports theory that trees growing in dense forests are competing for resources, reducing individual
409 tree leaf area (Jump et al., 2017). The negative relationships between height and α and positive relationships

410 between CAI and α relationships in our model suggest that trees may initially invest in vertical growth to reach
411 the canopy level, and once there invest in lateral growth, with more leaf area, to increase light capture. This
412 supports theory that trees grow to outcompete neighbouring individuals for light capture (Purves and Pacala, 2008)
413 and evidence that both lateral growth and LAI are reduced beneath closed canopies (Beaudet and Messier, 1998;
414 Canham, 1988).

415 Wood may be harder to accurately classify than leaves in TLS data (Vicari et al., 2019), resulting in a higher
416 occurrence of false positives in wood clouds, potentially leading to an overestimation in WAI, and therefore
417 underestimation of α , especially in trees with small leaves which are prevalent in dry, Mediterranean environments
418 (Peppe et al., 2011). The problem of misclassification will increase in taller trees due to TLS beam divergence,
419 occlusion and larger beam footprint at further distances (Vicari et al., 2019), suggesting that WAI overestimation
420 could be more pronounced in tall trees. Although our dense scanning strategy (Owen et al., 2021) was designed
421 to mitigate some of these effects, these effects mean our findings may underestimate the slope of the negative
422 relationship between α and tree height. Conversely, the increasing leaf-to-wood ratio could potentially be
423 explained by a greater number of empty voxels caused by occlusion in large trees. However, we took significant
424 steps to reduce occlusion, employing a 10 m scanning strategy that was developed in a dense tropical forest
425 (Wilkes et al., 2017).

426 **4.4 Correcting for non-photosynthetic elements in LAI estimates using TLS**

427 The value of TLS data to estimate individual tree PAI, WAI and subsequently α , demonstrates their potential to
428 corrective factors for non-photosynthetic components in ground based remote sensing measurements of LAI.
429 Properly correcting for WAI in LAI estimates is of global importance as small errors in ground based
430 measurements propagate through to large scale satellite observations generating large errors in global vegetation
431 models (Calders et al., 2018). The work presented here provides a foundation for future work combining multi-
432 source and multi-scale remote sensing datasets to correct largescale LAI products. Our results echo others' in
433 finding that the prevalence of woody material in the tree canopy, and therefore α , is dynamic and varies by species
434 as well as senescence, crown health and, in the case of deciduous forests, leaf phenology (Gower et al., 1999).
435 The use of single α value in a plot or region (Olivas et al., 2013; Woodgate et al., 2016), invariant of species, size
436 and forest structure, to convert PAI to LAI is therefore problematic (Niu et al., 2021). Our study demonstrates the
437 importance of taking species mix and structural variation into account when correcting for non-photosynthetic
438 material in ground-based LAI estimates.

439 **5. Conclusions**

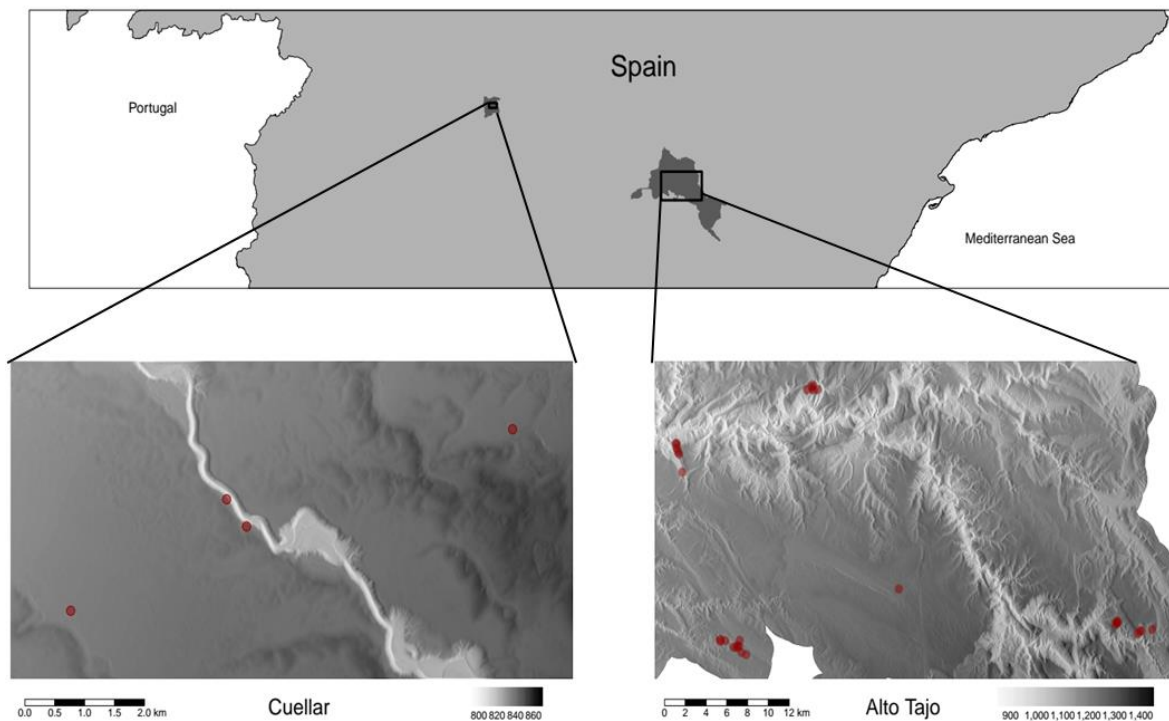
440 We tested three methods for estimating PAI using Terrestrial Laser Scanning data and compared these against
441 traditional DHP measurements. We found large variation between PAI values estimated from each TLS method
442 and DHP, demonstrating that care should be taken when deriving PAI from ground based remote sensing methods.
443 Although the *LiDAR Pulse* method was found to have the best agreement with both single scan and whole plot
444 PAI values measured by DHP, the *Voxel-Based* method allowed separate analysis of the key metric used to correct
445 for the effect of WAI in LAI measurements, α , in individual trees. We recommend the *LiDAR Pulse* method as a
446 fast and effective method for PAI estimation independent of illumination conditions. Whilst the *Voxel-Based*
447 method may be used to analyse individual tree α and determine ecological drivers of variation, work remains to

448 determine the validity of these approaches, in particular correct voxel size choice. We found that α varies by
449 species, height and stand density, showing the importance of accurately correcting for WAI on the individual tree
450 level and the utility of TLS to do so.

451 The variation in our results for the different methods used to derive PAI from TLS data show that there is some
452 way to go before TLS derived vegetation indices can be interpreted as robust and reliable. Validation using
453 destructive samples and further intercomparison studies of methods are needed to demonstrate the advantages of
454 TLS, and use of benchmarking datasets should be standard. DHP is a faster, cheaper and more widely accessible
455 method for PAI estimation, and while TLS promises to alleviate potential bias in DHP estimates, results are highly
456 methods dependent. Our results demonstrate the challenges that stand in the way of large scale adoption of TLS
457 for vegetation indices monitoring.

458 **6. Appendices**

459 **6.1 Appendix A**



460 **Figure A1: Map of plot locations within two field sites in central Spain (Cuellar, left and Alto Tajo, right). Red points**
461 **show plot locations on high-resolution digital terrain models enhanced with hillshading shown in greyscale (Owen.,**
462 **2021).**

463

464

465

466

467

468 **6.2 Appendix B**

469 **Table B1:** species – α linear mixed model (equation 1) showing relationship between tree species and α for all 2472
 470 individual trees. Species are listed from low – high drought tolerance, with the exception of *P. pinaster*, for which
 471 drought tolerance index has not been calculated in the literature. 95% CI are the 95% confidence intervals.

Species	α (eq. 1)	95% CI
<i>P. sylvestris</i>	0.144	0.131, 0.158
<i>P. nigra</i>	0.138	0.127, 0.149
<i>Q. faginea</i>	0.149	0.140, 0.157
<i>Q. ilex</i>	0.155	0.146, 0.166
<i>P. pinaster</i>	0.168	0.145, 0.192

472

473 **Table B2:** height – α linear mixed models for each species (equation 2) showing relationship between tree height and
 474 plot CAI and α for all 2472 individual trees. Species are listed from low – high estimated α . Significance codes: p <
 475 0.001 ‘***’; p < 0.01 ‘**’; p < 0.05 ‘*’; not significant ‘ns’. 95% CI are the 95% confidence intervals and ICC is the
 476 intra-class correlation coefficient.

Species	b (eq. 2) (95% CI)	c (eq. 2) (95% CI)	ICC
<i>P. sylvestris</i>	-0.002 ^{ns} (-0.004, 0.000)	0.134 ^{ns} (0.010, 0.259)	0.151
<i>P. nigra</i>	-0.005*** (-0.006, -0.004)	0.164** (0.063, 0.263)	0.211
<i>Q. faginea</i>	-0.008*** (-0.010, -0.007)	0.058* (0.016, 0.101)	0.060
<i>Q. ilex</i>	-0.015*** (-0.020, -0.011)	0.113** (0.050, 0.179)	0.070
<i>P. pinaster</i>	-0.006*** (-0.008, -0.004)	0.317* (0.177, 0.453)	0.036

477

478 **6.3 Appendix C**

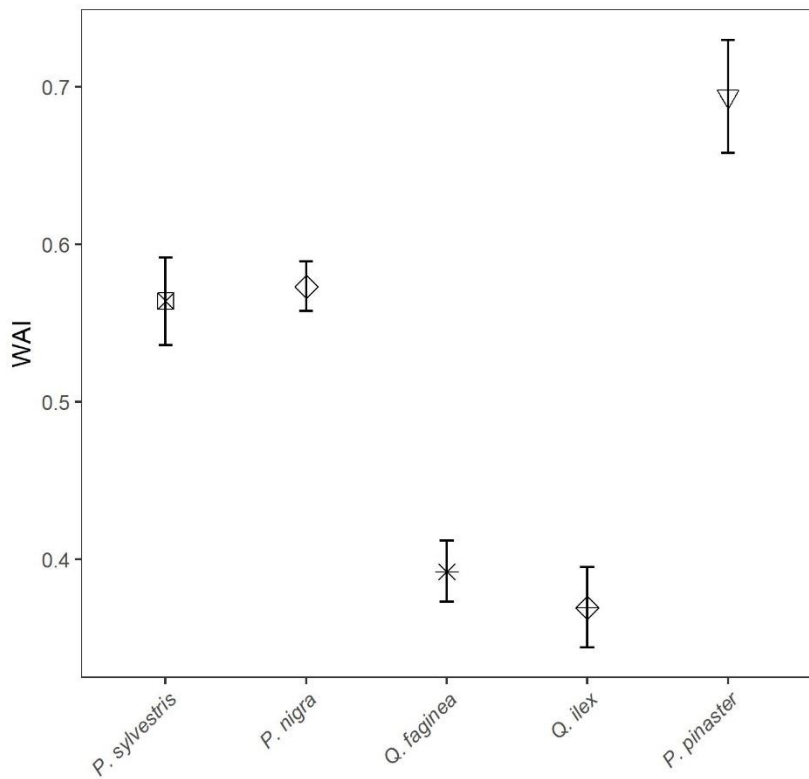
479 $WAI = m_{species}$ (C1)

480 $WAI = m \text{ height} + b$ (C2)

481 $WAI = m \text{ CAI} + b$ (C3)

482 $WAI = m \text{ PAI} + b$ (C4)

483 Where WAI is the wood area index, *species*, *height*, *CAI* and *PAI* are the tree species, tree height, crown area
 484 index of the plot in which the tree is growing and tree plant area index respectively and *m* and *b* are parameters to
 485 be fit.



486

487 **Figure C2:** Linear model derived WAI values (m, equation C1) for all 2472 individual trees of species *P. sylvestris*, *P.*
 488 *nigra*, *Q. faginea*, *Q. ilex* and *P. pinaster*. Error bars represent 95% confidence intervals. Species are listed from low –
 489 high drought tolerance, with the exception of *P. pinaster*, for which drought tolerance index has not been calculated in
 490 the literature. Between-species differences in WAI are likely primarily driven by differences in average tree height.

491 **Table C3:** Linear model (equation C1) showing relationship between tree species and WAI for all 2471 individual trees.
 492 Significance codes: p < 0.001 ‘***’; p < 0.01 ‘**’; p < 0.05 ‘*’; not significant ‘ns’. 95% CI are the 95% confidence
 493 intervals.

Species	m (eq. 1)	95% CI
<i>P. nigra</i>	0.57***	0.56, 0.59
<i>P. pinaster</i>	0.69***	0.66, 0.73
<i>P. sylvestris</i>	0.56(ns)	0.54, 0.59
<i>Q. faginea</i>	0.39***	0.37, 0.41
<i>Q. ilex</i>	0.37***	0.34, 0.39

494

495 **Table C4:** Linear models (equations C2, C3, C4) predicting WAI as a function of tree height, CAI (density) and PAI
 496 Significance codes: p < 0.001 ‘***’; p < 0.01 ‘**’; p < 0.05 ‘*’; not significant ‘ns’. 95% CI are the 95% confidence
 497 intervals.

	m (eq. 2, 3, 4) (95% CI)	b (eq. 2, 3, 4) (95% CI)	R ²
Tree Height	0.024*** (0.023, 0.026)	0.27*** (0.25, 0.28)	0.27
CAI	0.390*** (0.336, 0.443)	0.29*** (0.26, 0.31)	0.78
PAI	0.112*** (0.106, 0.118)	0.12*** (0.10, 0.14)	0.35

498

499 7. Code availability

500 See https://github.com/will-flynn/tls_dhp_pai.git for all processing and modelling code.

501 **8. Data availability**

502 See Owen et al. (2022) for individual segmented tree data and Flynn et al. (2023) for thresholded DHP images.

503 **9. Author contribution**

504 All authors designed the study. HJFO and WRMF collected and processed TLS and DHP data; WRMF performed
505 formal analysis with guidance from all authors. WRMF led the writing with input from all authors. All authors
506 contributed critically to drafts and gave final approval for publication.

507 **10. Competing interests**

508 The authors declare that they have no conflict of interest.

509 **11. Acknowledgements**

510 WRMF was funded through a London NERC DTP PhD studentship. ERL, HJFO and SWDG were funded through
511 the UKRI Future Leaders Fellowship awarded to ERL (MR/T019832/1).

512 **References**

513 Baeten, L., Verheyen, K., Wirth, C., Bruelheide, H., Bussotti, F., Finér, L., Jaroszewicz, B., Selvi, F.,
514 Valladares, F., Allan, E., Ampoorter, E., Auge, H., Avăcăriei, D., Barbaro, L., Bărnoaiea, I., Bastias, C. C.,
515 Bauhus, J., Beinhoff, C., Benavides, R., Benneter, A., Berger, S., Berthold, F., Boberg, J., Bonal, D.,
516 Brüggemann, W., Carnol, M., Castagneyrol, B., Charbonnier, Y., Chečko, E., Coomes, D., Coppi, A., Dalmaris,
517 E., Dănilă, G., Dawud, S. M., de Vries, W., De Wandeler, H., Deconchat, M., Domisch, T., Duduman, G.,
518 Fischer, M., Fotelli, M., Gessler, A., Gimeno, T. E., Granier, A., Grossiord, C., Guyot, V., Hantsch, L.,
519 Hättenschwiler, S., Hector, A., Hermy, M., Holland, V., Jactel, H., Joly, F.-X., Jucker, T., Kolb, S., Koricheva,
520 J., Lexer, M. J., Liebergesell, M., Milligan, H., Müller, S., Muys, B., Nguyen, D., Nichiforel, L., Pollastrini, M.,
521 Proulx, R., Rabasa, S., Radoglou, K., Ratcliffe, S., Raulund-Rasmussen, K., Seiferling, I., Stenlid, J., Vesterdal,
522 L., von Wilpert, K., Zavala, M. A., Zielinski, D., and Scherer-Lorenzen, M.: A novel comparative research
523 platform designed to determine the functional significance of tree species diversity in European forests,
524 *Persepect. Plant. Ecol.*, 15, 281–291, <https://doi.org/10.1016/j.ppees.2013.07.002>, 2013.

525 Baret, F., Weiss, M., Lacaze, R., Camacho, F., Makhmara, H., Pacholczyk, P., and Smets, B.: GEOV1: LAI and
526 FAPAR essential climate variables and FCOVER global time series capitalizing over existing products. Part1:
527 Principles of development and production, *Remote Sens. Environ.*, 137, 299–309,
528 <https://doi.org/10.1016/j.rse.2012.12.027>, 2013.

529 Bates, D., Mächler, M., Bolker, B., and Walker, S.: Fitting Linear Mixed-Effects Models Using lme4, *J. Stat. Softw.*, 67, <https://doi.org/10.18637/jss.v067.i01>, 2015.

531 Battaglia, M., Cherry, M. L., Beadle, C. L., Sands, P. J., and Hingston, A.: Prediction of leaf area index in
532 eucalypt plantations: effects of water stress and temperature, *Tree Physiol.*, 18, 521–528,
533 <https://doi.org/10.1093/treephys/18.8-9.521>, 1998.

534 Beaudet, M. and Messier, C.: Growth and morphological responses of yellow birch, sugar maple, and beech
535 seedlings growing under a natural light gradient, *Can. J. Forest Res.*, 28, 1007–1015,
536 <https://doi.org/10.1139/x98-077>, 1998.

537 Béland, M., Baldocchi, D. D., Widlowski, J.-L., Fournier, R. A., and Verstraete, M. M.: On seeing the wood
538 from the leaves and the role of voxel size in determining leaf area distribution of forests with terrestrial LiDAR,
539 *Agr. Forest Meterol.*, 184, 82–97, <https://doi.org/10.1016/j.agrformet.2013.09.005>, 2014.

540 Breda, N. J. J.: Ground-based measurements of leaf area index: a review of methods, instruments and current
541 controversies, *J. Exp. Bot.*, 54, 2403–2417, <https://doi.org/10.1093/jxb/erg263>, 2003.

542 Burt, A., Disney, M., and Calders, K.: Extracting individual trees from lidar point clouds using treeseg, *Methods Ecol. Evol.*, 10, 438–445, <https://doi.org/10.1111/2041-210X.13121>, 2019.

544 Calders, K., Armston, J., Newnham, G., Herold, M., and Goodwin, N.: Implications of sensor configuration and
545 topography on vertical plant profiles derived from terrestrial LiDAR, *Agr. Forest Meterol.*, 194, 104–117,
546 <https://doi.org/10.1016/j.agrformet.2014.03.022>, 2014.

547 Calders, K., Origo, N., Disney, M., Nightingale, J., Woodgate, W., Armston, J., and Lewis, P.: Variability and
548 bias in active and passive ground-based measurements of effective plant, wood and leaf area index, *Agr. Forest
549 Meterol.*, 252, 231–240, <https://doi.org/10.1016/j.agrformet.2018.01.029>, 2018.

550 Calders, K., Adams, J., Armston, J., Bartholomeus, H., Bauwens, S., Bentley, L. P., Chave, J., Danson, F. M.,
551 Demol, M., Disney, M., Gaulton, R., Krishna Moorthy, S. M., Levick, S. R., Saarinen, N., Schaaf, C., Stovall,
552 A., Terryn, L., Wilkes, P., and Verbeeck, H.: Terrestrial laser scanning in forest ecology: Expanding the
553 horizon, *Remote Sensing of Environment*, 251, 112102, <https://doi.org/10.1016/j.rse.2020.112102>, 2020.

554 Canham, C. D.: Growth and Canopy Architecture of Shade-Tolerant Trees: Response to Canopy Gaps, *Ecology*,
555 69, 786–795, <https://doi.org/10.2307/1941027>, 1988.

556 Carter, J. L. and White, D. A.: Plasticity in the Huber value contributes to homeostasis in leaf water relations of
557 a mallee Eucalypt with variation to groundwater depth, *Tree Physiol.*, 29, 1407–1418,
558 <https://doi.org/10.1093/treephys/tpp076>, 2009.

559 Caspersen, J. P., Vanderwel, M. C., Cole, W. G., and Purves, D. W.: How Stand Productivity Results from Size-
560 and Competition-Dependent Growth and Mortality, *PLoS ONE*, 6, e28660,
561 <https://doi.org/10.1371/journal.pone.0028660>, 2011.

562 Castro-Díez, P., Villar-Salvador, P., Pérez-Rontomé, C., Maestro-Martínez, M., and Montserrat-Martí, G.: Leaf
563 morphology and leaf chemical composition in three *Quercus* (Fagaceae) species along a rainfall gradient in NE
564 Spain, *Trees*, 11, 127–134, <https://doi.org/10.1007/PL00009662>, 1997.

565 Chen, J. M. and Black, T. A.: Defining leaf area index for non-flat leaves, *Plant Cell Environ.*, 15, 421–429,
566 <https://doi.org/10.1111/j.1365-3040.1992.tb00992.x>, 1992.

567 Coomes, D. A., Holdaway, R. J., Kobe, R. K., Lines, E. R., and Allen, R. B.: A general integrative framework
568 for modelling woody biomass production and carbon sequestration rates in forests, *Journal of Ecology*, 100, 42–
569 64, <https://doi.org/10.1111/j.1365-2745.2011.01920.x>, 2012.

570 Disney, M.: Terrestrial LiDAR: a three-dimensional revolution in how we look at trees, *New Phytol.*, 222,
571 1736–1741, <https://doi.org/10.1111/nph.15517>, 2018.

572 Flynn, W. R. M., Owen, H. J. F., Grieve, S. W. D., and Lines, E. R.: DHP images collected from Alto Tajo and
573 Cuellar in Spain. (V1), <https://doi.org/10.5281/ZENODO.7628072>, 2023.

574 Gazal, R. M., Scott, R. L., Goodrich, D. C., and Williams, D. G.: Controls on transpiration in a semiarid riparian
575 cottonwood forest, *Agr. Forest Meterol.*, 137, 56–67, <https://doi.org/10.1016/j.agrformet.2006.03.002>, 2006.

576 Gower, S. T., Vogel, J. G., Norman, J. M., Kucharik, C. J., Steele, S. J., and Stow, T. K.: Carbon distribution
577 and aboveground net primary production in aspen, jack pine, and black spruce stands in Saskatchewan and
578 Manitoba, Canada, *J. Geophys. Res.*, 102, 29029–29041, <https://doi.org/10.1029/97JD02317>, 1997.

579 Gower, S. T., Kucharik, C. J., and Norman, J. M.: Direct and Indirect Estimation of Leaf Area Index, fAPAR,
580 and Net Primary Production of Terrestrial Ecosystems, *Remote Sens. Environ.*, 70, 29–51,
581 [https://doi.org/10.1016/S0034-4257\(99\)00056-5](https://doi.org/10.1016/S0034-4257(99)00056-5), 1999.

582 Grotti, M., Calders, K., Origo, N., Puletti, N., Alivernini, A., Ferrara, C., and Chianucci, F.: An intensity, image-
583 based method to estimate gap fraction, canopy openness and effective leaf area index from phase-shift terrestrial
584 laser scanning, *Agr. Forest Meterol.*, 280, 107766, <https://doi.org/10.1016/j.agrformet.2019.107766>, 2020.

585 Hardwick, S. R., Toumi, R., Pfeifer, M., Turner, E. C., Nilus, R., and Ewers, R. M.: The relationship between
586 leaf area index and microclimate in tropical forest and oil palm plantation: Forest disturbance drives changes in
587 microclimate, *Agr. Forest Meterol.*, 201, 187–195, <https://doi.org/10.1016/j.agrformet.2014.11.010>, 2015.

588 Hijmans, R. J.: raster: Geographic Data Analysis and Modeling R package version 3.5-21, <https://CRAN.R-project.org/package=raster>., 2022.

590 Hosoi, F. and Omasa, K.: Voxel-Based 3-D Modeling of Individual Trees for Estimating Leaf Area Density
591 Using High-Resolution Portable Scanning Lidar, *IEEE T. Geosci. Remote*, 44, 3610–3618,
592 <https://doi.org/10.1109/TGRS.2006.881743>, 2006.

593 Itakura, K. and Hosoi, F.: Voxel-based leaf area estimation from three-dimensional plant images, *J. Agric.
594 Meteorol.*, 75, 211–216, <https://doi.org/10.2480/agrmet.d-19-00013>, 2019.

595 Jonckheere, I., Fleck, S., Nackaerts, K., Muys, B., Coppin, P., Weiss, M., and Baret, F.: Review of methods for
596 in situ leaf area index determination, *Agr. Forest Meterol.*, 121, 19–35,
597 <https://doi.org/10.1016/j.agrformet.2003.08.027>, 2004.

598 Jonckheere, I. G. C., Muys, B., and Coppin, P.: Allometry and evaluation of in situ optical LAI determination in
599 Scots pine: a case study in Belgium, *Tree Physiol.*, 25, 723–732, <https://doi.org/10.1093/treephys/25.6.723>,
600 2005.

601 Jucker, T., Bouriaud, O., Avacaritei, D., Dănilă, I., Duduman, G., Valladares, F., and Coomes, D. A.:
602 Competition for light and water play contrasting roles in driving diversity-productivity relationships in Iberian
603 forests, *J. Ecol.*, 102, 1202–1213, <https://doi.org/10.1111/1365-2745.12276>, 2014.

604 Jump, A. S., Ruiz-Benito, P., Greenwood, S., Allen, C. D., Kitzberger, T., Fensham, R., Martínez-Vilalta, J.,
605 and Lloret, F.: Structural overshoot of tree growth with climate variability and the global spectrum of drought-
606 induced forest dieback, *Glob. Change Biol.*, 23, 3742–3757, <https://doi.org/10.1111/gcb.13636>, 2017.

607 Jupp, D. L. B., Culvenor, D. S., Lovell, J. L., Newnham, G. J., Strahler, A. H., and Woodcock, C. E.: Estimating
608 forest LAI profiles and structural parameters using a ground-based laser called 'Echidna(R)', *Tree Physiol.*, 29,
609 171–181, <https://doi.org/10.1093/treephys/tpn022>, 2008.

610 Kamoske, A. G., Dahlin, K. M., Stark, S. C., and Serbin, S. P.: Leaf area density from airborne LiDAR:
611 Comparing sensors and resolutions in a temperate broadleaf forest ecosystem, *Forest Ecol. Manag.*, 433, 364–
612 375, <https://doi.org/10.1016/j.foreco.2018.11.017>, 2019.

613 Kuusk, V., Niinemets, Ü., and Valladares, F.: A major trade-off between structural and photosynthetic
614 investments operative across plant and needle ages in three Mediterranean pines, *Tree Physiol.*, 38, 543–557,
615 <https://doi.org/10.1093/treephys/tpx139>, 2018.

616 Leblanc, S. G. and Chen, J. M.: A practical scheme for correcting multiple scattering effects on optical LAI
617 measurements, *Agr. Forest Meterol.*, 110, 125–139, [https://doi.org/10.1016/S0168-1923\(01\)00284-2](https://doi.org/10.1016/S0168-1923(01)00284-2), 2001.

618 Lecigne, B., Delagrange, S., and Messier, C.: Exploring trees in three dimensions: VoxR, a novel voxel-based R
619 package dedicated to analysing the complex arrangement of tree crowns, *Ann. Bot-London*, 121, 589–601,
620 <https://doi.org/10.1093/aob/mcx095>, 2018.

621 Li, S., Dai, L., Wang, H., Wang, Y., He, Z., and Lin, S.: Estimating Leaf Area Density of Individual Trees
622 Using the Point Cloud Segmentation of Terrestrial LiDAR Data and a Voxel-Based Model, *Remote Sens-Basel*,
623 9, 1202, <https://doi.org/10.3390/rs9111202>, 2017.

624 Li, Y., Guo, Q., Tao, S., Zheng, G., Zhao, K., Xue, B., and Su, Y.: Derivation, Validation, and Sensitivity
625 Analysis of Terrestrial Laser Scanning-Based Leaf Area Index, *Can. J. Remote Sens.*, 42, 719–729,
626 <https://doi.org/10.1080/07038992.2016.1220829>, 2016.

627 Lines, E. R., Fischer, F. J., Owen, H. J. F., and Jucker, T.: The shape of trees: Reimagining forest ecology in
628 three dimensions with remote sensing, *J. Ecol.*, 110, 1730–1745, <https://doi.org/10.1111/1365-2745.13944>,
629 2022.

630 Long, J. N. and Smith, F. W.: Leaf area - sapwood area relations of lodgepole pine as influenced by stand
631 density and site index., *Can. J. Forest Res.*, 18, 247–250, 1988.

632 López, R., Cano, F. J., Martin-StPaul, N. K., Cochard, H., and Choat, B.: Coordination of stem and leaf traits
633 define different strategies to regulate water loss and tolerance ranges to aridity, *New Phytol.*, 230, 497–509,
634 <https://doi.org/10.1111/nph.17185>, 2021.

635 Lovell, J. L., Jupp, D. L. B., van Gorsel, E., Jimenez-Berni, J., Hopkinson, C., and Chasmer, L.: Foliage Profiles
636 from Ground Based Waveform and Discrete Point Lidar, *SilviLaser*, 1–9, 2011.

637 Ma, L., Zheng, G., Eitel, J. U. H., Magney, T. S., and Moskal, L. M.: Determining woody-to-total area ratio
638 using terrestrial laser scanning (TLS), *Agr. Forest Meterol.*, 228–229, 217–228,
639 <https://doi.org/10.1016/j.agrformet.2016.06.021>, 2016.

640 Madrigal-González, J., Herrero, A., Ruiz-Benito, P., and Zavala, M. A.: Resilience to drought in a dry forest:
641 Insights from demographic rates, *Forest Ecol. Manag.*, 389, 167–175,
642 <https://doi.org/10.1016/j.foreco.2016.12.012>, 2017.

643 Magnani, F., Mencuccini, M., and Grace, J.: Age-related decline in stand productivity: the role of structural
644 acclimation under hydraulic constraints, *Plant Cell Environ.*, 23, 251–263, <https://doi.org/10.1046/j.1365-3040.2000.00537.x>, 2000.

645 Mencuccini, M.: The ecological significance of long-distance water transport: short-term regulation, long-term
646 acclimation and the hydraulic costs of stature across plant life forms, *Plant Cell Environ.*, 26, 163–182,
647 <https://doi.org/10.1046/j.1365-3040.2003.00991.x>, 2003.

649 Mencuccini, M. and Grace, J.: Climate influences the leaf area/sapwood area ratio in Scots pine, *Tree Physiol.*,
650 15, 1–10, <https://doi.org/10.1093/treephys/15.1.1>, 1995.

651 Monsi, M. and Saeki, T.: On the Factor Light in Plant Communities and its Importance for Matter Production,
652 *Ann. Bot-London*, 95, 549–567, <https://doi.org/10.1093/aob/mci052>, 1953.

653 Nakagawa, S., Johnson, P. C. D., and Schielzeth, H.: The coefficient of determination R² and intra-class
654 correlation coefficient from generalized linear mixed-effects models revisited and expanded, *J. R. Soc.*
655 *Interface*, 14, 20170213, <https://doi.org/10.1098/rsif.2017.0213>, 2017.

656 Niinemets, Ü. and Valladares, F.: Tolerance to shade, drought, and waterlogging of temperate northern
657 hemisphere trees and shrubs, *Ecol. Monogr.*, 76, 521–547, [https://doi.org/10.1890/0012-9615\(2006\)076\[0521:TTSDAW\]2.0.CO;2](https://doi.org/10.1890/0012-9615(2006)076[0521:TTSDAW]2.0.CO;2), 2006.

659 Niu, X., Fan, J., Luo, R., Fu, W., Yuan, H., and Du, M.: Continuous estimation of leaf area index and the
660 woody-to-total area ratio of two deciduous shrub canopies using fisheye webcams in a semiarid loessial region
661 of China, *Ecol. Indic.*, 125, 107549, <https://doi.org/10.1016/j.ecolind.2021.107549>, 2021.

662 Olivas, P. C., Oberbauer, S. F., Clark, D. B., Clark, D. A., Ryan, M. G., O'Brien, J. J., and Ordoñez, H.:
663 Comparison of direct and indirect methods for assessing leaf area index across a tropical rain forest landscape,
664 *Agr. Forest Meterol.*, 177, 110–116, <https://doi.org/10.1016/j.agrformet.2013.04.010>, 2013.

665 Owen, H. J. F., Flynn, W. R. M., and Lines, E. R.: Competitive drivers of inter-specific deviations of crown
666 morphology from theoretical predictions measured with Terrestrial Laser Scanning, *J. Ecol.*, 109, 2612–2628,
667 <https://doi.org/10.1111/1365-2745.13670>, 2021.

668 Owen, H. J. F., Flynn, W. R. M., and Lines, E. R.: Individual TLS tree clouds collected from both Alto Tajo and
669 Cuellar in Spain., 2022.

670 Peppe, D. J., Royer, D. L., Cariglino, B., Oliver, S. Y., Newman, S., Leight, E., Enikolopov, G., Fernandez-
671 Burgos, M., Herrera, F., Adams, J. M., Correa, E., Curran, E. D., Erickson, J. M., Hinojosa, L. F., Hoganson, J.
672 W., Iglesias, A., Jaramillo, C. A., Johnson, K. R., Jordan, G. J., Kraft, N. J. B., Lovelock, E. C., Lusk, C. H.,
673 Niinemets, Ü., Peñuelas, J., Rapson, G., Wing, S. L., and Wright, I. J.: Sensitivity of leaf size and shape to
674 climate: global patterns and paleoclimatic applications, *New Phytol.*, 190, 724–739,
675 <https://doi.org/10.1111/j.1469-8137.2010.03615.x>, 2011.

676 Pfeifer, M., Gonsamo, A., Disney, M., Pellikka, P., and Marchant, R.: Leaf area index for biomes of the Eastern
677 Arc Mountains: Landsat and SPOT observations along precipitation and altitude gradients, *Remote Sens.*
678 *Environ.*, 118, 103–115, <https://doi.org/10.1016/j.rse.2011.11.009>, 2012.

679 Phillips, N., Bond, B. J., McDowell, N. G., Ryan, M. G., and Schauer, A.: Leaf area compounds height-related
680 hydraulic costs of water transport in Oregon White Oak trees, *Funct. Ecol.*, 17, 832–840,
681 <https://doi.org/10.1111/j.1365-2435.2003.00791.x>, 2003.

682 Purves, D. and Pacala, S.: Predictive Models of Forest Dynamics, *Science*, 320, 1452–1453,
683 <https://doi.org/10.1126/science.1155359>, 2008.

684 Ridler, T. W. and Calvard, S.: Picture Thresholding Using an Iterative Selection Method, *IEEE T. Syst. Man.*
685 *Cyb.*, 8, 630–632, <https://doi.org/10.1109/TSMC.1978.4310039>, 1978.

686 Sea, W. B., Choler, P., Beringer, J., Weinmann, R. A., Hutley, L. B., and Leuning, R.: Documenting
687 improvement in leaf area index estimates from MODIS using hemispherical photos for Australian savannas,
688 *Agr. Forest Meterol.*, 151, 1453–1461, <https://doi.org/10.1016/j.agrformet.2010.12.006>, 2011.

689 Specht, R. L. and Specht, A.: Canopy structure in Eucalyptus-dominated communities in Australia along
690 climatic gradients, *Canopy structure in Eucalyptus-dominated communities in Australia along climatic*
691 gradients, 10, 191–213, 1989.

692 Vicari, M. B., Disney, M., Wilkes, P., Burt, A., Calders, K., and Woodgate, W.: Leaf and wood classification
693 framework for terrestrial LiDAR point clouds, *Methods Ecol. Evol.*, 10, 680–694, <https://doi.org/10.1111/2041-210X.13144>, 2019.

695 Warton, D. I., Wright, I. J., Falster, D. S., and Westoby, M.: Bivariate line-fitting methods for allometry, *Biol.*
696 *Rev.*, 81, 259–291, <https://doi.org/10.1017/S1464793106007007>, 2006.

697 Warton, D. I., Duursma, R. A., Falster, D. S., and Taskinen, S.: smatr 3 - an R package for estimation and
698 inference about allometric lines: *The smatr 3 - an R package*, *Methods Ecol. Evol.*, 3, 257–259,
699 <https://doi.org/10.1111/j.2041-210X.2011.00153.x>, 2012.

700 Weiss, M., Baret, F., Smith, G. J., Jonckheere, I., and Coppin, P.: Review of methods for in situ leaf area index
701 (LAI) determination, *Agr. Forest Meterol.*, 121, 37–53, <https://doi.org/10.1016/j.agrformet.2003.08.001>, 2004.

702 Whitehead, D.: The Estimation of Foliage Area from Sapwood Basal Area in Scots Pine, *Forestry*, 51, 137–149,
703 <https://doi.org/10.1093/forestry/51.2.137>, 1978.

704 Wilkes, P., Lau, A., Disney, M., Calders, K., Burt, A., Gonzalez de Tanago, J., Bartholomeus, H., Brede, B., and
705 Herold, M.: Data acquisition considerations for Terrestrial Laser Scanning of forest plots, *Remote Sensing of*
706 *Environment*, 196, 140–153, <https://doi.org/10.1016/j.rse.2017.04.030>, 2017.

707 Woodgate, W., Jones, S. D., Suarez, L., Hill, M. J., Armston, J. D., Wilkes, P., Soto-Berelov, M., Haywood, A.,
708 and Mellor, A.: Understanding the variability in ground-based methods for retrieving canopy openness, gap
709 fraction, and leaf area index in diverse forest systems, *Agr. Forest Meterol.*, 205, 83–95,
710 <https://doi.org/10.1016/j.agrformet.2015.02.012>, 2015.

711 Woodgate, W., Armston, J. D., Disney, M., Jones, S. D., Suarez, L., Hill, M. J., Wilkes, P., and Soto-Berelov,
712 M.: Quantifying the impact of woody material on leaf area index estimation from hemispherical photography
713 using 3D canopy simulations, *Agr. Forest Meterol.*, 226–227, 1–12,
714 <https://doi.org/10.1016/j.agrformet.2016.05.009>, 2016.

715 Zhang, Y., Chen, J. M., and Miller, J. R.: Determining digital hemispherical photograph exposure for leaf area
716 index estimation, *Agr. Forest Meterol.*, 133, 166–181, <https://doi.org/10.1016/j.agrformet.2005.09.009>, 2005.

717 Zheng, G., Moskal, L. M., and Kim, S.-H.: Retrieval of Effective Leaf Area Index in Heterogeneous Forests
718 With Terrestrial Laser Scanning, *IEEE T. Geosci. Remote*, 51, 777–786,
719 <https://doi.org/10.1109/TGRS.2012.2205003>, 2013.

720 Zhu, X., Skidmore, A. K., Wang, T., Liu, J., Darvishzadeh, R., Shi, Y., Premier, J., and Heurich, M.: Improving
721 leaf area index (LAI) estimation by correcting for clumping and woody effects using terrestrial laser scanning,
722 *Agr. Forest Meterol.*, 263, 276–286, <https://doi.org/10.1016/j.agrformet.2018.08.026>, 2018.

723